Journal of the European Ceramic Society **16** (1996) 353–365

0955-2219(95)00194-8
0955-2219/96/$15.00

Structure and Composition of Metal/Ceramic Interfaces

Manfred Rühle

Max-Planck-Institut für Metallforschung, Institut für Werkstoffwissenschaft, Seestrasse 92, D-70174 Stuttgart, Germany

(Received 11 September 1995; revised version received 31 October 1995; accepted 7 November 1995)

Abstract

The structure and composition of metal/ceramic interfaces play an important rôle for the properties of composites, for the bonding of bulk metals (or metallic alloys) to bulk ceramics, in electronic packaging, and for the properties of oxide scales on metals (or metallic alloys) formed after high-temperature corrosion. In this paper the possibilities of high-resolution transmission electron microscopy (HRTEM) and analytical electron microscopy (AEM) will be summarized and recent developments discussed. Those advancements encompass quantification of HRTEM data by image processing and studies of specific components of the interfaces by investigations of the near-edge fine structures (ELNES) of energy loss spectra. The techniques will be applied to the Nb/Al_2O_3, and Cu/Al_2O_3 interfaces, respectively.

1 Introduction

Metal/ceramic interfaces (MCI) belong to heterophase boundaries.[1] Those boundaries exist between two crystals which possess different structures and/or compositions. In contrast, a homophase boundary separates two crystals of the same material with the same composition (see Fig. 1). Recently, heterophase boundaries and MCIs were the subject of intense research and of several conferences.[2–4] The great interest in MCIs results from the high potential of application of those components: (i) for the bonding of metals to ceramics; (ii) as an important component of composites; (iii) electronic packaging systems used in information processing; (iv) thin film technology and (v) high-temperature oxidation of metals and metallic alloys. The MCIs must typically sustain mechanical and/or electrical forces without failure. Consequently, interfaces exert an important, sometimes controlling influence on performance for the components mentioned above.

A basic understanding of the properties of the interfaces requires a knowledge of the different structures and compositions of the MCIs. The structures should be available to the atomic level and the coordinates of atoms at or near to the interface have to be determined with high precision. At the interface between two dissimilar materials, segregation of impurities and/or the formation of reaction products may occur.[5–7] Those processes lead to a modification of the properties of the system. Therefore, it is essential to also study the composition and possible reactions at the MCI.

In this paper, results will be reported with respect to structural studies by *quantitative* high-resolution transmission electron microscopy (QHRTEM) as well as investigations on chemical processes and bonding across the interface by analytical electron microscopy (AEM), with emphasis on electron energy loss spectroscopy (EELS), and studies of the energy loss near edge structures (ELNES). The techniques will be applied to the Nb/Al_2O_3 and Cu/Al_2O_3 interface.

2 Remarks on Bonding Across Metal/Ceramic Interfaces

The free energy per unit area, γ, of an interface represents the most fundamental thermodynamic property of an interface. The free energy is correlated to the measurable work of adhesion W_{ad} by the Dupré equation[8]

$$W_{ad} = \gamma_m + \gamma_c - \gamma \quad (1)$$

with γ_m = surface energy of the metal and γ_c = surface energy of the ceramic. Attractive interaction between the two constituents (metal, ceramic) results in $W_{ad} > 0$.

The measurement of W_{ad} is not easy. Jilavi[9] determined W_{ad} by measuring contact angles at (equilibrium) pores present at the MCI following a suggestion by Fischmeister *et al.*[10] Jilavi determined W_{ad} for Nb/Al_2O_3 interfaces by TEM cross-sections of equilibrium pores in solid state bonded bicrystals. W_{ad} ranges from 0·5 to 1·5 J/m^2 depending on the relative orientation of the Nb single crystal with respect to the sapphire crystal.

homophase boundaries

grain boundaries

twins

domain boundaries

stacking faults

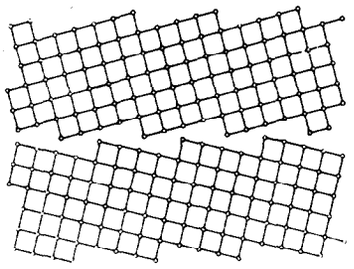

heterophase boundaries

M(I) / M(II)

ZrO_2 (t) / ZrO_2 (c)

Metal / Ceramic

Metal / Semiconductor

Metal / Polymer

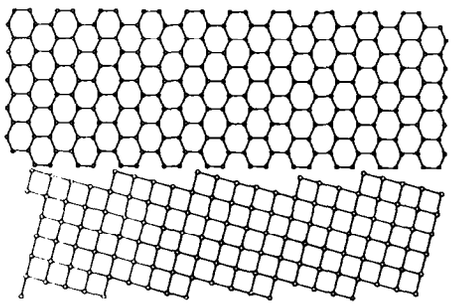

Fig. 1. Homophase boundaries and heterophase boundaries. Homophase boundaries limit on both sides materials of the same composition and same structure, whereas at heterophase boundaries the structure and/or composition of both components is different.

The evaluation is made by assuming an isotropic behaviour of all quantities in eqn (1). This is, however, not correct for most crystalline materials. Nevertheless, the measured data[9] result in the correct order of magnitude of W_{ad}. Furthermore, the anisotropy of the interface energies alone cannot explain the measured variation of W_{ad}.[9]

A theoretical description of W_{ad} on the atomic level requires the knowledge of the interatomic potential at the interface. At the MCI a *qualitative* change in the bonding across the interface occurs. There exist appropriate models for describing interatomic forces in the metal and in the ceramics, respectively.[11] However, an interatomic potential between a metal and a ceramic cannot be derived easily. Geometrical arguments do, in general, not lead to a correct description of the dependence of W_{ad} on orientation,[12] as suggested previously.[13] Cluster calculations[14] predicted the trend of W_{ad} for several MCIs, however, no quantitative or even semi-quantitative values of W_{ad} can be deduced from those simple calculations.

The phenomenological considerations are contrasted by recent fundamental calculations of the bonding across MCIs. *Ab initio* calculations of rather small cells containing the interface allow the determination of the bonding at MCIs. Those calculations were performed for Ag/MgO[15–17] and Nb/Al_2O_3.[18–20] In the calculations the Schrödinger equation is being solved without any input parameter but basic atomic data and an assumed structure of the selected cell containing up to about 50 atoms (ions) only. No structural relaxations are possible in the calculations. Therefore, the calculations have to be performed for different atomic arrangements and the energy determined. The lowest energy configuration represents the most likely configuration of the system. The calculations result in the electronic band structure of the ground state at 0 K.

In a first step, Kruse *et al.*[20] calculated the equilibrium structure of a Nb monolayer on a (0001) sapphire surface. Figure 2 shows the Nb positions of the different starting configurations used in the calculations. After different runs in the computer for different atomic configurations it could be proven that the absolute energy minimum of the Nb/Al_2O_3 interface occurs with Nb in the A position (Fig. 2). This result agrees with HRTEM observations of MBE grown Nb over layers on (0001) Al_2O_3.[21–24]

Basically the same result is obtained for bulk Nb (3–5 atomic layers of Nb on top of the (0001) sapphire surface).[18,19] The positions of all atoms (ions) can be calculated for the lowest energy configuration (Fig. 3). The results of the first-principles calculations allow detailed analysis of the bonding at the Nb/Al_2O_3 interface. Charge density plots (Fig. 4) reveal that the Nb atoms are partially ionized. At the same time, electron density accumulates between Nb and O atoms. Detailed analysis of the electron density distribution reveal that the increase of charge density is mainly an overlap of atomic orbitals, rather than delocalization of electrons into a molecular orbital.[19] This analysing leads to the conclusion that the bonding between Nb (monolayer and bulk) and sapphire is predominantly ionic. Charge is being transferred from the metal to the oxide leading to ionic bonding. Similar results are obtained for Ag/MgO.[15–17]

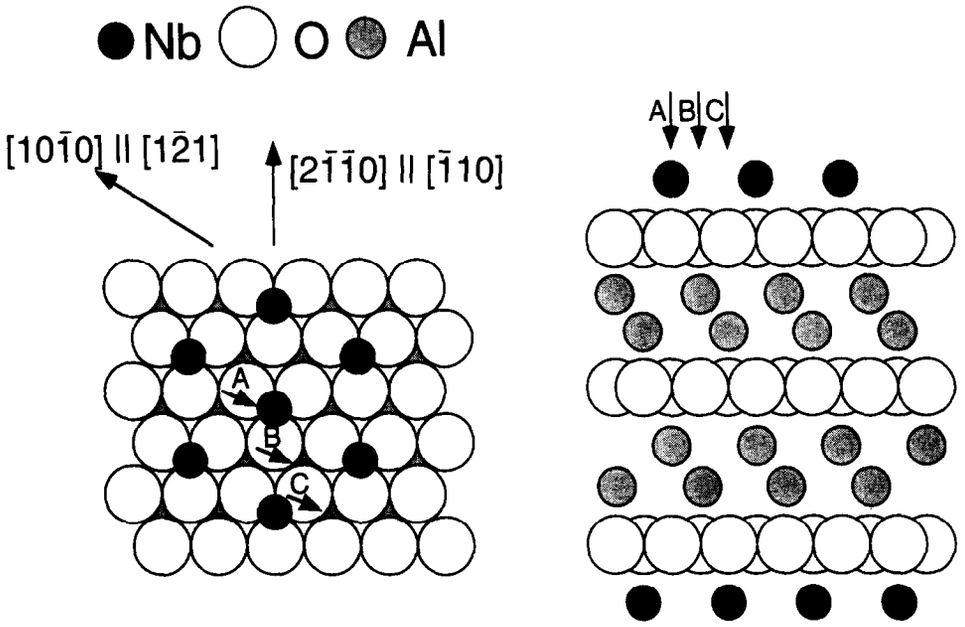

Fig. 2. Model of a Nb monolayer on the (0001) surface of sapphire used for the first-principles calculations of Kruse *et al.*[18-20] A, B and C denote those different positions of the Nb atoms for which the calculations have been done. (a) and (b) show the model in plan view and in cross-section, respectively.[20]

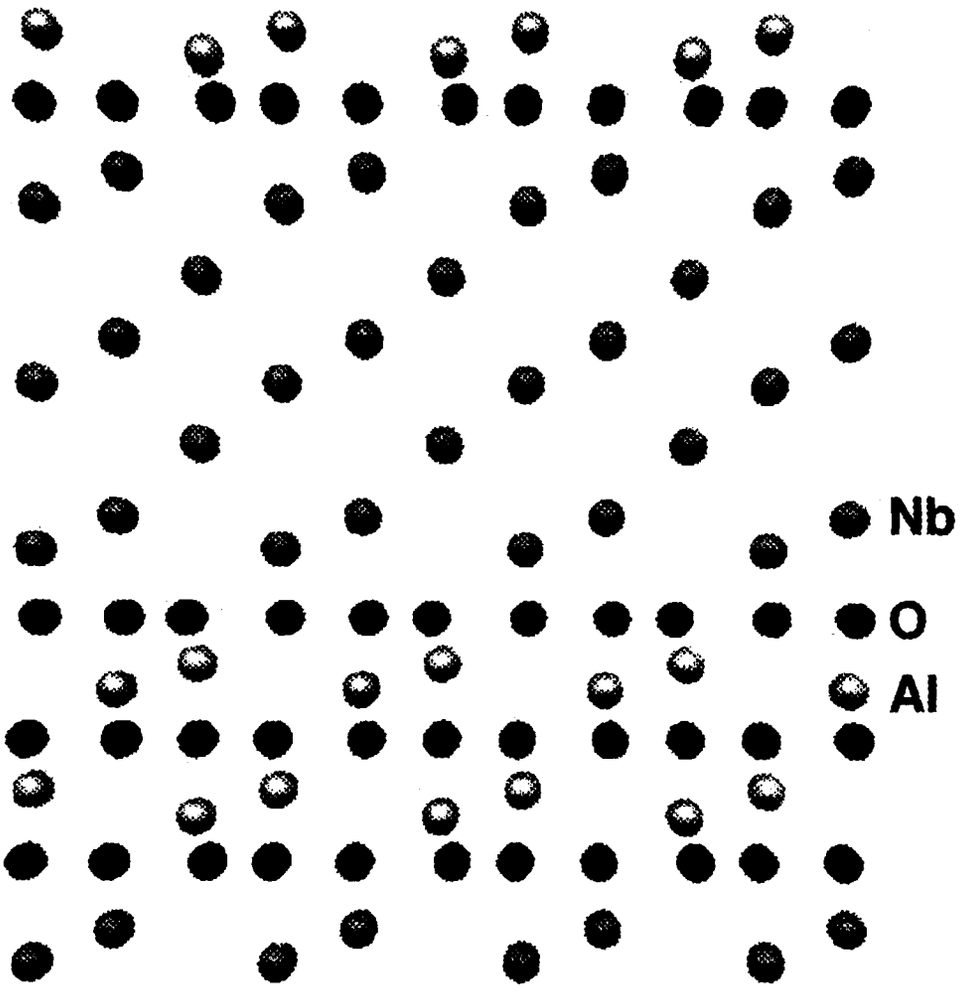

Fig. 3. Model of 'bulk' Nb on the (0001) surface of sapphire. A layer of 3 (or 5) Nb atoms on top of sapphire can be handled by the computer. A small kink in the 2nd Nb layer indicates the attractive forces on the Nb by Al_2O_3.[19]

So far *ab initio* calculations can only be performed for less than about 50 atoms. In these small supercells it is assumed that the metal (Nb, Ag) fits coherently to the oxide substrate. The mismatch between the two lattices (metal and ceramics, respectively) can so far not yet be treated on the same basic level since the required supercell cannot be calculated by today's computers.

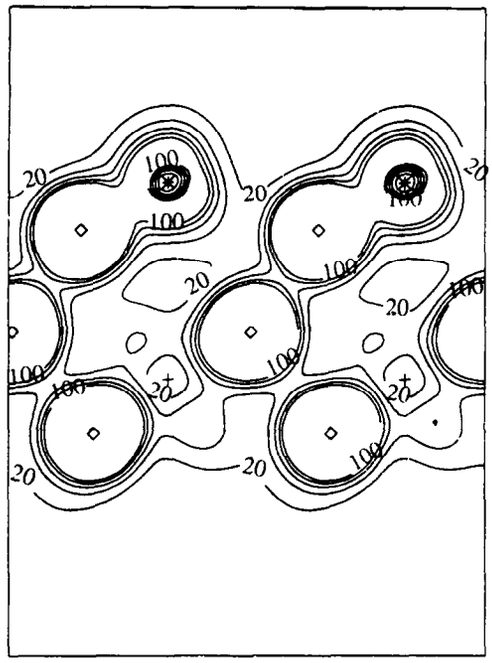

Fig. 4. Charge density (in units of 0·003 $e^{-}A^{-3}$) of a Nb monolayer on a (0001) sapphire slab, according to a self-consistent *ab initio* band structure calculations. The projection direction corresponds to $(2\bar{1}\bar{1}0)$ in sapphire. O, Al and Nb atoms (ions) are indicated by 0, + and *, respectively (C. Kruse *et al.*[18,20]).

Empirical interatomic potentials have to be used for modelling of the structure and misfit dislocations and the dislocation networks.[25] Experimentally, so far, different results are obtained by different authors.[26,27]

Korn *et al.*[28,29] have shown experimentally that the level of the bonding energy at the interface between Nb and Al_2O_3 can be strongly influenced by impurities and chemical processes occurring at the interface. However, no fundamental (basic) theory can so far explain the measured changes. Empirical models have to be used.

3 Transmission Electron Microscopy

The different possibilities offered by modern transmission electron microscopy are summarized schematically in Fig. 5.[30] Conventional TEM techniques (CTEM) involve bright field (BF) and dark field (DF) imaging and selected area diffraction (SAD). CTEM is being used for morphological analyses, the identification of different phases and for the analysis of lattice defects.[31] Spectroscopy can be performed in an analytical TEM with high spatial resolution.[32] The probe size in a scanning transmission electron microscopy (STEM) ranges from less than 1·0–50 nm. Energy dispersive spectroscopy (EDS) uses X-rays emitted from the specimen for a chemical characterization,[32] while characteristic energy losses can be used for identifying qualitatively and quantitatively the different elements present in the specimen by electron energy loss spectroscopy (EELS).[33] EELS has so far most successfully been applied for the analysis of light elements. The surroundings of atoms can be probed by extended energy-loss fine structure studies (EXELFS) whereas energy-loss near-edge structure (ELNES) investigations result in information on the distance, bonding and bonding states to neighbouring atoms.[34] ELNES has been successfully applied to interfaces.[35] High-resolu-

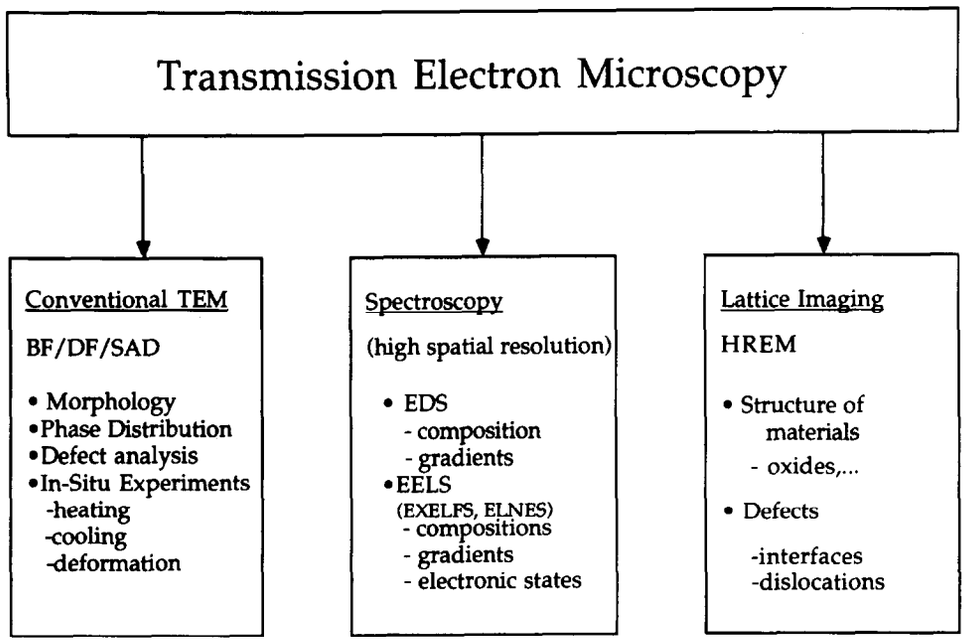

Fig. 5. Schematic illustrations of different TEM techniques. (a) Conventional TEM (CTEM), only one beam is used for imaging (BF: bright field imaging; DF: dark field imaging; SAD: selected area diffraction). (b) Spectroscopy utilizes the inelastic scattering processes of electrons in the specimen for a chemical characterization with high spatial resolution (EDS: energy dispersion spectroscopy; EELS: electron energy loss spectroscopy; EXELFS: extended energy-loss fine structure; ELNES: electron energy loss near-edge structure. (c) Lattice imaging. The direct and scattered beam from the image (HRTEM: high resolution transmission electron microscopy).

tion transmission electron microscopy (HRTEM) studies result in structure images[36–38] of small perfect and/or defected regions in crystal.

In this paper we concentrate on quantitative high-resolution transmission electron microscopy and advanced analytical electron microscopy studies. This emphasis should, however, not diminish the important role that conventional TEM still plays in materials science: most results obtained so far in electron microscopy are done in the area of CTEM.

4 Determination of Atomic Structure of Metal/Ceramic Interfaces by Quantitative High-Resolution Transmission Electron Microscopy

The resolution of commercially available transmission electron microscopes has improved significantly. The point-to-point resolution of medium high-voltage electron microscopes with an acceleration voltage of 300–400 kV results in ~0·17 nm. The new generation of high-voltage high-resolution instruments pushes the resolution limit to ~0·1 nm.[39]

The major obstacle in applying HRTEM routinely in materials science is caused by the fact that experimentally obtained micrographs cannot be interpreted in a 'naive way', which means that, for example, dark spots on a micrograph correspond to the position of a column of atoms in the investigated specimen.[36,37] On the contrary, the contrast on a micrograph is formed by a complex scattering procedure which usually excludes the naive interpretation.

If one assumes that a completely coherent plane wave enters the specimen at the upper specimen surface then the amplitude and phase of the wave field at the exit surface can be calculated following well established procedures. The dynamical scattering of electrons is complex and highly nonlinear which means that the wavefield does not depend linearly on any experimental parameter such as specimen thickness and specimen orientation and positions of atoms or columns of atoms.[36,37]

Furthermore, the HRTEM image depends on several instrumental parameters such as: (i) the coherency of the illumination system. (ii) The spherical aberration of rotational symmetric lenses which cannot be corrected. This aberration results in a change of the phase of the electron wave scattered even under small angles (≤ 1°, depending on the instrument). This alteration may lead to a modification of the experimentally recorded micrograph. (iii) The exact position of the imaging plane (with respect to the exit surface of the specimen), the defocus value Δf, is an additional parameter which can be adjusted and has to be known rather accurately for a proper interpretation of the experimental micrograph. (iv) Finally, the recording medium (photographic film, CCD camera, etc.) influences also the registered micrograph.

Another important, although nearly trivial aspect is that a HRTEM micrograph represents a two-dimensional (2D) projection of a three-dimensional (3D) object. Detailed information can be obtained if the specimen is crystalline and is oriented so that the incoming electron beam is parallel to a low-order Laue zone. A determination of the coordinates of an atom in a specimen requires experimental studies in (at least) two different orientations ('electron tomography'[40]). For one HRTEM analysis of crystalline materials, the number and location of the positions of atom column rows can be established. For the analysis it is assumed that the lattice to be investigated is periodic in the direction of the incoming beam. The analysis of the atomistic structure of an interface requires that a low indexed zone axis of both crystals adjacent to the interface and the interface itself are parallel to the incoming electron beam. (See Fig. 7).

The amplitude and intensity distribution in the image plane depends critically on the spherical aberration of the objective lens. The geometrical beam path is shown in Fig. 6(a). In the image plane of the objective plane, an image of the object is formed by the interference of the transmitted beam with all diffracting beams. A better physical description of the image-forming processes can be performed by using wave optics (Fig. 6(b)). A transmission function $q(x, y)$ leaves the exit surface of the crystalline specimen. This

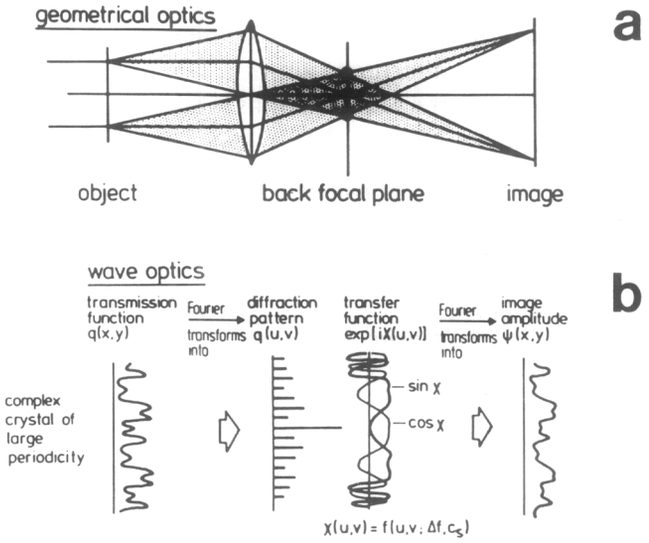

Fig. 6. Image formation by the objective lens of a transmission electron microscopy. (a) Geometric optical path diagram (b) Wave optical description (see text for explanation). Contrast transfer CTF = $\exp(i\chi(u,v))$, with $\chi(u,v) = f(u,v,\Delta f,C_s)$. u,v: Coordinates in the diffraction plane, Δf: defocus distance (= distance between lower specimen surface and imaging plane); C_s: constant of spherical aberration.

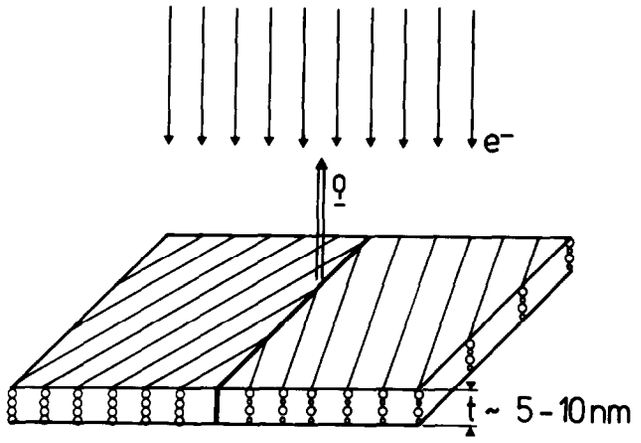

Fig. 7. Direct imaging of an interface by HRTEM. The crystalline specimen must be adjusted so that the direction of the incoming electron beam coincides with the orientation of atomic columns. The schematic drawing includes an interface. HRTEM can successfully be performed at such an interface if the interface normal lies perpendicular to the direction of the incoming beam (or the interface plane parallel to the direction of the incoming beam). Note that the foil thickness has to be in the range of 5–10 nm. The foil thickness should be constant over the investigated area.

function $q(x, y)$ can be periodic or non-periodic. The wave field moves through the objection lens and the amplitude distribution in a diffraction pattern $Q(u, v)$ is formed by a Fourier transformation of $q(x, y)$. The intensity distribution in the diffraction plane $Q(u, v)$ is being modified according to the exact shape of the contrast transfer function (CTF) of the microscope.[36] A Fourier back transformation of the modified amplitude distribution $Q(u, v)$ leads to the amplitude and intensity distribution in the image plane of the objective plane. Owing to the strong modifications caused by the CTF the amplitude and plane distribution in the image plane can be dramatically altered compared to the wave field leaving the specimen.

Quantitative interpretation of a HRTEM micrograph of the perfect specimen as well as of a specimen containing a lattice defect (such as an interface)

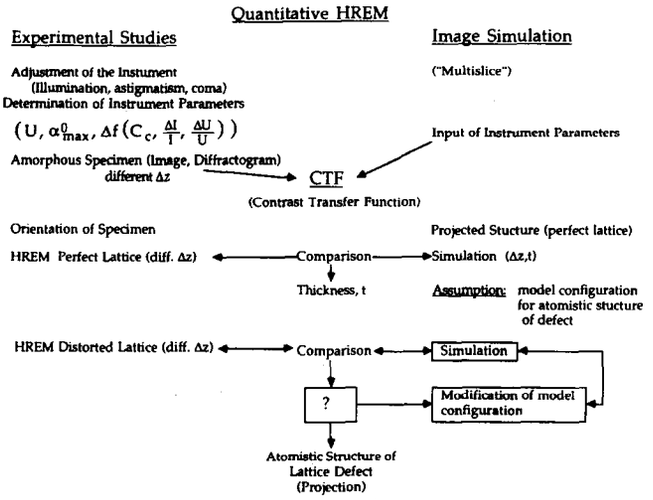

Fig. 8. A flow chart for quantitative high-resolution transmission electron microscopy (QHRTEM).

requires two independent steps (Fig. 8). Firstly, experimental micrographs have to be taken under well defined imaging conditions and the electron microscope has to be aligned and the contrast transfer function (CTF) has to be determined.[41] The interpretation of the micrographs requires the knowledge of the exact thickness of the specimen. This is usually done by comparing the experimental micrographs (taken under different focus values) with simulated images (for different thicknesses and defocus values). A quantitative comparison results in both values, the thickness and the defocus distance Δf. Often it is helpful to reduce the noise on the micrograph. This can best be done by an adaptive Fourier filtering technique.[42]

The second step covers the quantitative analysis of the nature and position of atomic columns at or near the defect such as an MCI. The analysis requires that a series of micrographs is taken under different, well defined defocus values. The experimental micrographs have to be compared to simulated image. For the simulated images a model configuration of the atomistic structure of the crystal (including the lattice defect) has to be assumed.

The simulated images have to be compared to experimental micrographs. So far most authors made the comparison with a visual inspection. The experimental micrograph and the simulated image are shown side by side. Sometimes, the mounting of an inlet of the simulated image into an experimental micrograph should demonstrate the 'good agreement'. This evaluation is, however, not quantitative. The accuracy of critical parameters (volume increase at an interface, positions of atomic columns at or near defect) cannot be determined objectively.

Recently, techniques for a quantitative evaluation of HRTEM micrographs have been developed.[43,44] These techniques use advanced image processing techniques for the evaluation of HRTEM micrographs. Firstly, the experimental micrograph is noise reduced.[42] Then the experimental micrograph as well as the simulated image are stored in a computer pixel by pixel (usually 1024 × 1024 pixels). After aligning and bringing both images to the same magnification, the two images are subtracted from each other. If there would be full agreement between the experimental micrograph and the simulated image, then the sum of intensity differences in corresponding pixels would be zero. This is usually not the case. There exists always a residual intensity (difference intensity). It is essential that this difference intensity does not contain any structural information and consists completely of noise. If the residual intensity of the difference image is significantly different from zero, then the positions of columns

in the atomistic model are varied, an image is simulated and the difference image is formed again by subtracting the modified simulated image from the experimental micrograph. This procedure is continued until best agreement between the experimental micrograph and simulated image is reached.[43,44]

There exists different measures of agreement between two micrographs.[45] The normalized Euclidian distance (NED) is an excellent measure for comparing two images. NED is defined as

$$NED = \frac{\sqrt{\sum_p \{I_1(p) - I_2(p)\}^2}}{\sqrt{\sum_p I_1(p)^2} \cdot \sqrt{\sum_p I_2(p)^2}} \quad (2)$$

where the summations contain the intensities I of the pixels labelled p. The subscript 1 corresponds to the experimental micrograph and the subscript 2 to the simulated image. Best agreement is reached when the NED is as small as possible (ideally equal to zero). Information on the accuracy can be obtained from the value of NED.[44] This technique was applied for the determination of the structure of unknown materials as well as of the structure of grain boundaries and MCIs. The procedure requires a lot of computer time.

5 Analytical Electron Microscopy

When an electron beam passes through a specimen there exists always a nonvanishing cross-section for inelastic scattering processes which leads to an energy distribution of the electrons passing through the specimen. The energy losses can be subdivided into the zero-loss region 0(< ΔE < eV), plasmon region (ΔE < 100 eV) and core-loss region. From the different regions one can get information on the chemistry and bonding of the specimen.[33,34] Plasmon losses result from the collective excitation of electrons, whereas the core-loss regions (edges) result from energy losses caused by the excitation of electrons from inner shells. The minimum energy required to eject an electron from an inner shell is specific for every element. Therefore, this energy can be used for a characterization of elements present in the specimen. Techniques exist for the quantification of the data.[32-34] In addition, the fine structure of edges (ELNES) allows the determination of the bonding and distances to nearest neighbour atoms.[34]

6 Case Study 1: Structure of Nb/Al_2O_3 Interface

The interface between Nb and sapphire serves as a model system for MCIs since both constituents are representative materials: Nb as a bcc metal and Al_2O_3 as a technologically important ceramic. Since Al and O are highly soluble in Nb, no reaction products form at the interface. Thermal stresses can be neglected because the thermal expansion coefficients of Nb and sapphire are about the same.

The accommodation of the lattice mismatch between a thin film and its substrate is an important concern in thin film technology. The lattice mismatch can be compensated by straining the lattice of the film or by misfit dislocations. Straining the epilayer leads to coherent interfaces, whereas the presence of misfit dislocations leads to semicoherent interfaces. At semicoherent interfaces, coherent regions exist between the misfit dislocations. The atomistic structure of the coherent regions and the misfit dislocations were studied by quantitative HRTEM. Additional information on bonding at the interface can be obtained by ELNES studies (see Section 6.3).

6.1 Experimental details and results

The Nb layers were grown in a MBE growth chamber as described elsewhere.[46,21,23,24] During the growth of the Nb films the substrate was heated to 1123 K and a vacuum of 10^{-6} Pa was maintained. A typical growth rate was 1 monolayer/s. The film thicknesses ranged from 12 to 100 nm. Most HRTEM studies were performed at a JEOL 4000 EX with a point resolution of 0·17 nm. Some studies were performed at the Berkeley ARM[21] and the Stuttgart ARM.[23]

X-ray and electron diffraction revealed that a unique orientation relationship exists between the Nb and the Al_2O_3 lattices for all investigated interfaces. The orientation relationship can be described by the following sets of parallel directions in the two crystals: $[0001]_S \parallel [111]_{Nb}$ and $[2\bar{1}\bar{1}0]_S \parallel [1\bar{1}0]_{Nb}$ (S = sapphire). The lattice planes in the Nb and sapphire lattice, which are parallel to the interface, are thus given by the orientation relationship and the chosen substrate surface: $(0001)_S \parallel (111)_{Nb}$, $(01\bar{1}0)_S \parallel (11\bar{2})_{Nb}$, $(2\bar{1}\bar{1}0)_S \parallel (1\bar{1}0)_{Nb}$ and $(01\bar{1}\,2)_S \parallel (0\ 0\ 1)_{Nb}$. The different interfaces are referred to as system 1, system 2, system 3 and system 4, respectively, in the following text.

6.2 Atomistic structure of the coherent regions

The quantitative evaluation of the HRTEM micrographs of the interfaces shows that the atomistic structure in the coherent regions of all four interfaces can be described by the same building principle. Two simple rules characterize the building principle for these interfaces. As an example, the evaluation of a HRTEM micrograph of the interface of system 1 is described. Figure 9(a) shows a

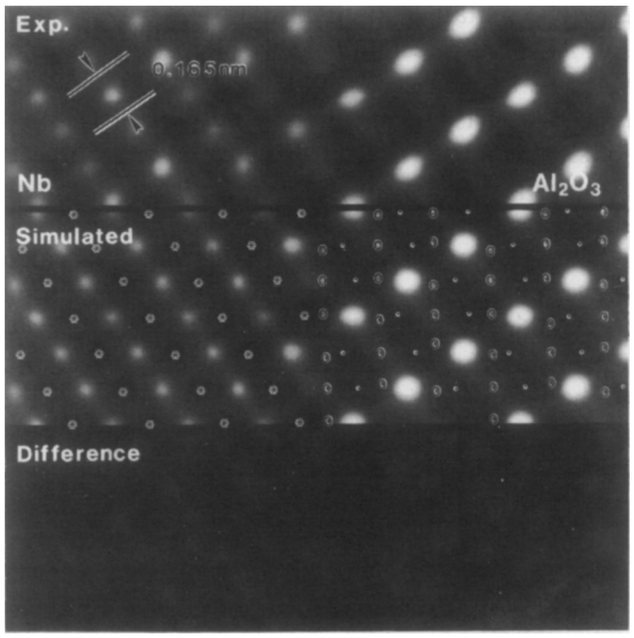

Fig. 9. HRTEM micrograph of the Nb/Al_2O_3 interface. (a) Experimental micrograph, I_e. (b) Simulated image based on the interface shown in Fig. 10(a), I_s. (c) Difference image $D = |I_e - I_s|$. The positions of columns of atoms (ions) can be determined quantitatively. Summary of results, see Table 1.

HRTEM micrograph of the interface of system 1 taken along the $[2\bar{1}\bar{1}0]_S$ and $[1\bar{1}0]_{Nb}$ directions. The intensity distribution on the micrograph is given by $I(x, y)_e$, where x and y are the coordinates of pixels on the experimental micrograph. Figure 9(b) represents a simulated image of the interface model of Fig. 10(a). The corresponding calculated intensity distribution is given by $I(x, y)_s$. Figure 9(c) contains the difference image $D = |I_e - I_s|$. The sum of the intensities in all pixels in D is minimized by the procedure described in Section 4 (eqn (2)). The experimentally determined structure is shown in Fig. 10(a) and the determined parameters are summarized in Table 1.

All Nb atoms at this interface occupy Al lattice sites. The translation vector T (Fig. 10) is thus a lattice vector of the sapphire lattice. The Nb atoms at the interface of all other systems also continue the Al lattice of the sapphire. This leads to the first rule, which states that a maximum of Al lattice sites is occupied by Nb atoms. This rule

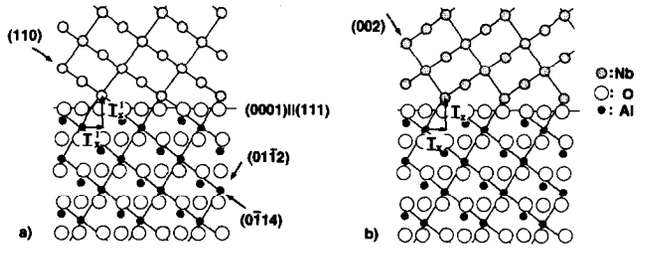

Fig. 10. (a) Nb/Al_2O_3 interface model which results in the best agreement between simulated image and experimental micrograph. (b) Interface model with the Nb lattice in a twin orientation with respect to the Nb lattice of Fig. 10(a).

Table 1. Structure of Nb/Al_2O_3 interface — results by quantitative HREM

Translation state (perfect Nb to perfect Al_2O_3)	T = (–0·1,–0·1) Å, ±0·1 Å
Terminating layer of Al_2O_3	Oxygen
Relaxation of first Nb layer	R_1 = (–0·2,–0·1) Å, ±0·1 Å
Relaxation of other Nb layer i	R_i = (0·0) Å, ±0·1 Å
Kink in Nb lattice	No

is confirmed by the coincidence of the morphological unit cell of sapphire,[47] which is rhombohedral (a = 85·7°, a = 0·35 nm) and constructed by connecting Al lattice sites, and the bcc unit cell of Nb (a = 0·33 nm).[24] If only the position of the Nb atoms of the first layer were determined, then twins should occur in the Nb lattice of system 1 and 2. These twins have never been observed. Figure 10(b) shows an interface model for system 1 with the Nb lattice in a twin orientation with respect to the Nb lattice as shown in Fig. 9 and Fig. 10(a). Thus the position of the Nb atoms in the second layer must be fixed. The second rule states that the Nb atoms of the second layer occupy positions, which are close to the Al lattice sites of a continued Al lattice of the sapphire. The second rule also explains the rotation of the Nb lattice of system 4 in a specific direction.[24] It is interesting that so far the theoretically predicted kink in the second Nb layer (see Fig. 3) cannot be observed experimentally by HRTEM. Further theoretical and experimental studies have to be performed.

A quantitative evaluation of the HRTEM micrographs does not reveal unequivocally the nature of the terminating plane of sapphire. The terminating layer could either be composed of Al or Nb. Both would agree with the HRTEM micrograph analysed so far. As will be shown in the next section, ELNES studies support the model with an oxygen terminating layer.

6.3 Electron energy loss near edge structures (ELNES) studies

ELNES studies of characteristic edges have been performed[48] for the energy losses close to an energy edge. Using a dedicated scanning transmission electron microscope (STEM) Bruley *et al.*[48] record EELS spectra at high spatial resolution. A spectrum of a 'box' with a size of 3 × 4 nm^2 is taken from areas including the interfaces and then a spectrum is taken from pure Nb and sapphire. It is assumed that the signal of the total spectrum $I_T(\Delta E)$ which, taken from the area which includes the interface, is linearly composed of components resulting from the two crystals adjacent to the interface (I_{Nb} and I_S, respectively) and from the interface area itself, I_I.

$$I_T(\Delta E) = a\, I_I(\Delta E) + b \cdot I_{Nb}(\Delta E) + c \cdot I_S(\Delta E). \quad (3)$$

The interface-specific component of the ELNES was obtained by using the spatial difference technique as described in Section 6.3.[48] For this method three spectra were acquired, one from a region containing the interface and two in the adjacent bulk materials. The interface spectrum contained not only the signal from the interfacial atoms but also contributions from the surrounding bulk materials. The extraction of the interfacial ELNES requires the removal of the contributions from the bulk materials. The reference spectra taken in the bulk materials were scaled and then subtracted from the interface spectrum. The remaining difference spectrum represents the ELNES arising from the interfacial atoms with an environment or oxidation state different from both bulk materials. The scaling of the reference spectra is necessary because different numbers of bulk atoms are irradiated during the acquisition of the interface and reference spectra respectively. The scaling factors were determined by trial and error applying the following guidelines: Selection of an energy-loss region containing strong and characteristic features for the bulk materials and minimizing these contributions in the difference spectrum. In the case that a chemical shift occurs, the intensity directly above the edge onset is eliminated. Care was taken that the subtraction of the reference spectra did not lead to negative intensities which are physically not allowed.

The quantities a, b, c are constants which have to determined from reference spectra.[48] The O–K-edge and the Nb–M-edge were studied. (Fig. 11) It could be concluded that the interface term I_I contains a signal which must result from Nb being in an oxidized state (Nb^{3+}) whereas Al exists only with Al^{3+} configuration. Those investigations suggest that sapphire is terminated by an oxygen layer and the first Nb layer (of the Nb crystal) consists of oxidized Nb. Those observations are in agreement with the results of *ab initio* calculations.[18–20]

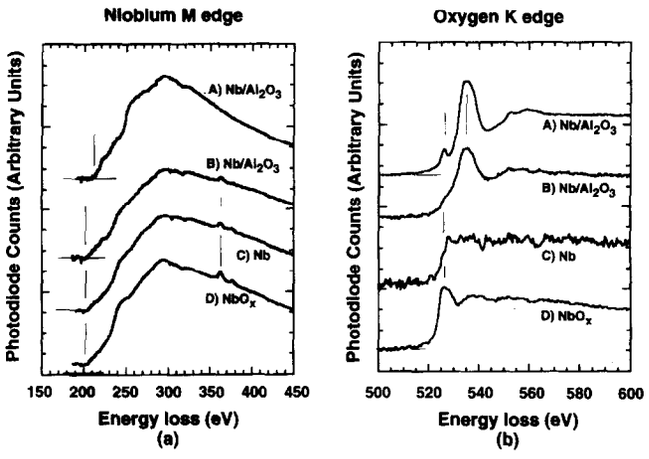

Fig. 11. Energy loss near edge structure (ELNES) of the regions at or close to the Nb/Al_2O_3 interface. (a) O–K-edge. The different spectra are recorded at various locations across the interface. A reference spectra for NbO_x and Nb is shown. The little peak visible at the spectrum taken from the interface region is indicative of Nb^{3+}. Nb must form the terminating layer. (b) Al_2O_3, L-edge. There exist no difference the ELNES of the interface and bulk A indicating that Al atoms 'feel' always the same environment. Al does not terminate the sapphire.

6.4 Misfit dislocations at the interface

The Burgers vector of the misfit dislocations are determined by a Burgers circuit in the HRTEM micrograph. An example for a Burgers circuit around a misfit dislocation of system 4 is shown in Fig. 12. The Burgers circuit results in a Burgers vector of 1/2 [11$\bar{1}$]. The edge component 1/2 [110] is parallel to the interface and accommodates the lattice mismatch. The edge component 1/2 [00$\bar{1}$] is perpendicular to the interface and causes the rotation of the Nb lattice. Due to the rotation of the Nb lattice, the $(001)_{Nb}$ planes are not parallel to the $(01\bar{1}2)_S$ interface plane. Table 2 summarizes the experimental results for all systems.[23,27] Burgers vector components, which do not accommodate any lattice mismatch, are in general compensated in these networks. In the network of system 2 and 4, these components are compensated by an alternating sequence of misfit dislocations with the same line direction but different Burgers vectors. Only the 1/2 [00$\bar{1}$] Burgers vector component of the misfit dislocations of system 4 with line direction [1$\bar{1}$0] is not compensated. In the network of system 1, the edge component b_{perp} perpendicular to the interface of one array of dislocations is compensated by the b_{perp} component of the second array.

The Burgers vector of the misfit dislocations has been determined with HRTEM due to the small average distance d_{MD} between the misfit dislocations. If d_{MD} is smaller than 1/3 of the extinction

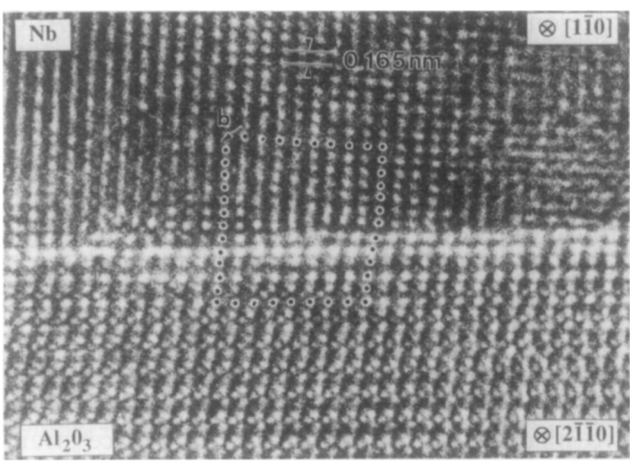

Fig. 12. HRTEM micrograph of a misfit dislocation at the Nb/Al_2O_3 interface of system 4. A Burgers circuit is marked around a misfit dislocation. The micrograph is not yet evaluated quantitatively.

Table 2. Summary of the dislocation networks

System	*Line direction*	*Burgers vector*	*Edge dislocation*	*Geometry*	d_{MD}
System 1	$\xi_1 = [1\bar{1}0]$	$\vec{b}_1 = 1/2[11\bar{1}]$	+	rhombic	21 nm
(0001) ‖ (111)	$\xi_2 = [01\bar{1}]$	$\vec{b}_2 = 1/2[1\bar{1}\bar{1}]$	+		21 nm
System 2	$\xi_1 = [1\bar{1}0]$	$\vec{b}_1 = 1/2[111]$	+	rectangular	2·4 nm
$(01\bar{1}0) \parallel (11\bar{2})$	$\xi_2 = [111]$	$\vec{b}_{2a} = 1/2[1\bar{1}1]$	−		12·1 nm
		$\vec{b}_{2b} = 1/2[1\bar{1}\bar{1}]$	−		
System 3	$\xi_1 = [11\bar{2}]$	$\vec{b}_1 = 1/2[111]$	+		14 nm
$(2\bar{1}\bar{1}0) \parallel (1\bar{1}0)$	$\xi_2 = [112]$	$\vec{b}_2 = 1/2[11\bar{1}]$	+		2·5 nm
System 4	$\xi_1 = [1\bar{1}0]$	$\vec{b}_{1b} = 1/2[11\bar{1}]$	+	rectangular	2·7 nm
$(01\bar{1}2) \parallel (001)$	$\xi_2 = [110]$	$\vec{b}_{2a} = 1/2[1\bar{1}1]$	+		12·1 nm
		$\vec{b}_{2b} = 1/2[1\bar{1}\bar{1}]$	+		

distance ξg, then it is impossible to distinguish between the contrast of a dislocation network and a moiré pattern.[49] The extinction distance $\xi[110]$ for Nb is 26 nm.

7 Case Study 2: The Copper/Sapphire Interface

7.1 The structure of the Cu/Al_2O_3 interface

Cu films were deposited on Al_2O_3 substrates in a MBE machine. During the growth of the crystal reflection high energy electron diffraction patterns could be observed. It was quite interesting that at a growth temperature of 473 K only a ring pattern could be revealed (with reflection from {111}, {200}, {220}, {311} and {422} Cu planes). After depositing a certain thickness of Cu the crystallites reorient and form a single crystalline film. The diffraction ring pattern remains unchanged up to an effective film thickness of about 10 nm. But for thicknesses beyond 10 nm the RHEED pattern develops sharp diffraction streaks characteristic of single crystal films. The close packed planes and the close-packed directions in the two crystals are parallel:

$$(111)_{Cu} \parallel (0001)_S \text{ and } <110>_{Cu} \parallel [10\bar{1}0]_S \qquad (4)$$

Edge-on bright field imaging of the Cu/Al_2O_3 interface reveals a sharp transition between the sapphire substrate and the Cu layer. No chemical reaction on interdiffusion has occurred at the interface during crystal growth. Theoretical calculations[14] indicate that Cu bonds to surface oxygen atoms (ions) of sapphire. The approximate 7% difference between the corresponding spacing of the adjacent lattices raises the question of coherence at the Cu/Al_2O_3 interface.

Either the lattice strain of the film is relaxed by a network of misfit dislocations, or contact of the two phases does not introduce any lattice strain. For the case of a semicoherent interface, two different hexagonal misfit dislocation networks are possible.[50] One network consists of 60° dislocations with $<110>_{Cu}$ line vectors which should be observable end-on in a HRTEM lattice image such as Fig. 13. This HRTEM micrograph of the Cu/Al_2O_3 interface was obtained with the incident beam parallel to $[10\bar{1}0]Al_2O_3$ and $<110>_{Cu}$, respectively. The dominant periodicity of sapphire in the lattice image corresponds to the spacing of $(2\bar{1}\bar{1}0)$ Al_2O_3 and $(0003)Al_2O_3$ planes. The $(0003)Al_2O_3$ planes are parallel to the $\{\bar{1}10\}$Cu planes. Since the copper lattice is slightly twisted about $[\bar{1}11]$Cu, the contribution of the $\{1\bar{1}1\}$Cu planes is weak whereas (002)Cu planes are dominant. The experimental image does not reveal localized misfit dislocations, thus the less likely case of a 60° misfit dislocation network is excluded.

The other possible misfit dislocation network has edge type dislocations with a $a_{Cu}/2$ $<110>_{Cu}$ Burgers vectors and line vectors along $<211>_{Cu}$ directions. Thus a network will be visible by imaging the Cu/Al_2O_3 interface edge-on the [211]Cu direction. In order to resolve the $\{220\}_{Cu}$ planes with a lattice spacing of 1·28 Å, the experimental image shown in Fig. 13 was obtained on the Stuttgart-ARM.[39] The resolved $(022)_{Cu}$ planes do not reveal any trace of strain fields caused by the proposed dislocation network. Additionally, no periodicity between the terminating copper and sapphire planes is found. Therefore, the investigated Cu/Al_2O_3 interfaces can be described by a rigid lattice model possessing an incoherent interface. The weak adhesion of copper on sapphire based on non-covalent bonding[14] and also the absence of localized misfit dislocations for internally oxidized copper/alumina interfaces,[50] agrees well with the results of these investigations.[51]

7.2 Energy loss spectroscopy at the Cu/Al_2O_3 interface

Each absorption edge in EELS is associated with an energy-loss near-edge structure (ELNES) which contains information on bonding and electronic structure.[34] Different oxidation states of metals can be distinguished either by a change in the energy onset of a particular edge (a so called chemical shift) and/or by a change in the shape of the ELNES. The latter is also sensitive to the local

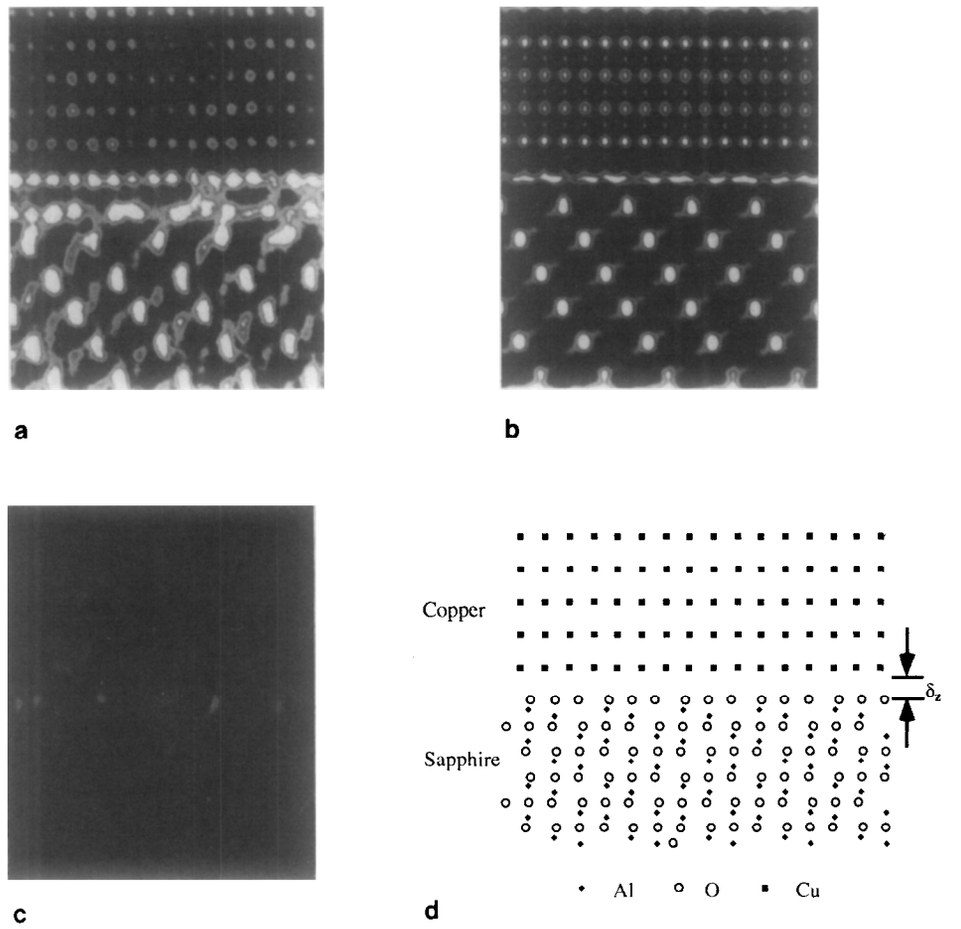

Fig. 13. (a) HRTEM micrograph of the Cu/Al_2O_3 interface. (ARM Stuttgart). The (022) planes of Cu can readily be seen (0·12 nm distance). A detailed analysis revealed that a fixed orientation relationship exists between Cu and Al_2O_3. The interface is, however, incoherent. (b) Simulated micrograph assuming the atomistic model of Fig. 13(d). (c) Difference image $D = |I_e - I_s|$. (d) Model used for image shown in Fig. 13(b) (G. Dehm, unpublished work).

coordination of the atomic species. In this section, results on ELNES of Cu/Al_2O_3 interfaces are reported. The same specimens as for the structural studies were used.

The measurements were carried out with a VG HB 501 dedicated STEM spectrometer (Gatan 666 PEELS) as described in Section 6.3. Scanning the beam enables simultaneous imaging of the interface and allows a manual correction of specimen drift. All spectra were corrected for dark current and readout-pattern of the parallel detector. The pre-edge background was extrapolated by a power law $A \times E^{-r}$ [33] and subtracted from the original data.

The interface-specific component of the ELNES was obtained by using the spatial difference technique as described in Section 6.3.[48] For this method three spectra were acquired, one from a region containing the interface and two in the adjacent bulk materials. The interface spectrum contains not only the signal from the interfacial atoms but also contributions from the surrounding bulk materials. The extraction of the interfacial ELNES requires the removal of the contributions from the bulk materials. The reference spectra taken in the bulk materials were scaled and then subtracted from the interfaces spectrum. The remaining difference spectrum represents the ELNES arising from the interfacial atoms with an environment or oxidation state different from both bulk materials. The scaling of the reference spectra is necessary because different numbers of bulk atoms are irradiated during the acquisition of the interface and reference spectra respectively. The scaling factors were determined by trial and error applying the following guidelines: selection of an energy-loss region containing strong and characteristic features for the bulk materials and minimizing these contributions in the difference spectrum. In the case that a chemical shift occurs, the intensity directly above the edge onset is eliminated. Care was taken that the subtraction of the reference spectra did not lead to negative intensities which are physically not allowed.

The $Cu–L_{2,3}$ edge spectra recorded in the bulk copper and at the Cu/Al_2O_3 interface are shown in Fig. 14. The spectrum taken in the bulk sapphire is omitted because there is only a smooth background in this energy-loss region. Subtraction of the $Cu–L_{2,3}$ edge spectrum of bulk copper from the interface spectrum yields a difference spectrum

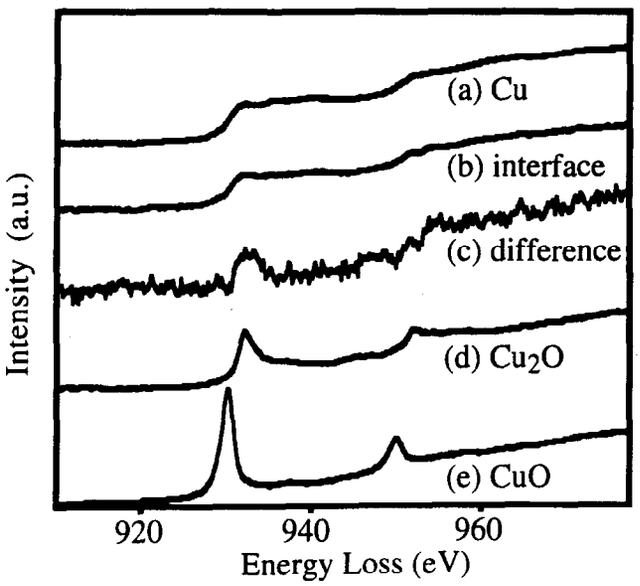

Fig. 14. ELNES studies at Cu/Al_2O_3 interface. $Cu–L_{2,3}$ edge of (a) Cu; (b) the interface containing region; (c) the extracted difference spectrum; (d) Cu_2O and (e) CuO. The position and shape of the maximum in (c) is similar as in (d) suggesting that at the interface Cu^+ exists. (C. Scheu, unpublished results).

with an ELNES different from the pure metal (Fig. 14). The difference spectrum shows a shape similar to the reference spectra taken from cuprous oxide (Cu_2O) and cupric oxide (CuO) (Fig. 14(d, e)). No chemical shift, typical for Cu^{2+}, was observed, which indicates that Cu exists at the interface in a Cu^{1+} oxidation state.

The ELNES of the $Al–L_{2,3}$ edge in bulk sapphire (onset 78 eV) and the $Cu–M_{2,3}$ edge in bulk copper (onset 74 eV) overlap. Therefore, the spectrum measured at the interface contains contributions from both bulk materials. The intensity of the calculated difference spectrum is zero within the detection limits set by noise. This indicates that the Al atoms are not involved in the bonding and that no noticeable change in the local coordination of the Al atoms occurs. From the results of the $Cu–L_{2,3}$ edge one might expect a change of the $Cu–M_{2,3}$ ELNES which was not observed.

The results of the investigation of the $Cu–L_{2,3}$ and $A–L_{2,3}$ edge indicate an interaction between the Cu and the O atoms, whereas the Al atoms are not affected by the presence of the interface. This is supported by the existence of a difference spectrum at the O–K edge. The interface-specific component shows a slight downward shift of the edge onset and a broadening of the main peak at 540 eV compared to the O–K edge in the sapphire matrix.

Using the basic formulae for the quantification of an EELS absorption edge[33,34]

$$S = J_0 N \sigma \tag{5}$$

(S = characteristic inner-shell signal; J_0 = total transmitted intensity; N = number of atoms per unit area, and σ = cross section) it is possible to obtain the number of atoms affected by the interface. The interfacial width is the region containing these interfacial atoms with a coordination or oxidation state different from both bulk materials. From the ratio of the signal of the difference spectrum and the as-acquired interface spectrum both integrated over an energy-loss region of 30 eV above the edge onset a width of $0{\cdot}36 \pm 0{\cdot}04$ nm is obtained (averaged over ten measurements in two different specimens). This corresponds to 1·6 monolayers when compared to the 0·21 nm spacing of the Cu (111) planes which are parallel to the interface.

The ELNES of the $Cu–L_{2,3}$, O–K and $Al–L_{2,3}$ edge of the Cu/Al_2O_3 interface indicate bonding between copper and the oxygen sublattice of α-Al_2O_3 with a charge transfer from copper to oxygen. The oxidation state of copper at the interface is +1. The aluminium atoms do not alter their coordination compared to bulk α-Al_2O_3. The results show that the investigation of the interfacial ELNES is a useful method to study the bonding and electronic structure of metal/ceramic interfaces.

If segregated atoms exist at the MCIs interfaces they could be identified by AEM. For example, it is readily possible to determine segregation of components by EDS technique and EELS. The detection limit is in the order of 1.

Acknowledgements

The author acknowledges many helpful discussions with J. Bruley, G. Dehm, F. Ernst, M. W. Finnis, G. Gutekunst, C. Kruse, J. Mayer, C. Scheu and H. Müllejans. The work was supported by the Volkswagen Foundation (contract monitor Dr H. Steinhardt) under contract no. I/66 791.

References

1. Cahn, J. W. & Kalonji, G., *Solid–solid phase transformation*, ed. H. I. Aaronson, American Society for Metals, Metals Park/OH, 1982, p. 1.
2. Rühle, M., Evans, A. G., Ashby, M. F. & Hirth, J., (eds), *Metal/Ceramic Interfaces, Acta-Scripta Metall.* Proc. Series Vol. 4, Pergamon Press, Oxford, 1989.
3. Rühle, M., Heuer, A. H. & Ashby, M. F., Metal/ceramic interfaces. Suppl. *Acta Metall. Mater.*, **40** (1992)S1–368.
4. Knowles, K. M., Microscopy of interface in composites. *J. Microscopy*, **169** (1993) 95; **177** (1995) 187.
5. Trumble, K. P. & Rühle, M., *Acta Metall. Mater.*, **39** (1991) 1915.
6. Ernst, F. & Rühle, M., Materials Science Forum, **155/156** (1994) 331.
7. Ernst, F., *Mat. Sci. Eng.*, **R14** (1995) 97.
8. Klomp, J. T., *Ceramic Microstructure 86: Role of Interfaces*, eds J. A. Pask & A. G. Evans, Plenum Press, New York, 1986, p. 307.

9. Jilavi, M., Ph.D. Thesis, Universität of Stuttgart, 1995.
10. Fischmeister, H. F., Navara, E. & Easterling, K. E., *Mat. Sci.*, **6** (1972) 211.
11. Sutton, A. P. & Balluffi, R. W., *Interfaces in Crystalline Materials*, Clarendon Press, Oxford (1995).
12. Sutton, A. P. & Balluffi, R. W., *Acta Metall. Mater.*, **35** (1987) 2177.
13. Fecht, H. J. & Gleiter, H., *Acta Metall. Mater.*, **33** (1985) 557.
14. Johnson, K. H. & Pepper, S. V., *J. Appl. Phys.*, **53** (1982) 6634.
15. Li, R., Wu, Q., Freeman, A. J. & Fu, C. L., *Phys. Rev.*, **B48** (1993) 8317.
16. Schönberger, U., Andersen, O. K. & Methfessel, M., *Acta Metall. Mater.*, **40** (1992) S1.
17. Hong, T., Smith, J. R. & Srolovitz, D. J., *Acta Metall. Mater.*, **43** (1995) 2721.
18. Kruse, C., Ph.D Thesis, Universität Stuttgart, 1994.
19. Finnis, M. W. & Kruse, C., *Materials at High Temperatures*, **12** (1994) 189; *Proc. Mat. Res. Soc. Symp.*, **357** (1995) 427.
20. Kruse, C., Finnis, M. W., Milman, V. Y., Payman, M. C., Vita, A. D. & Gillan, M. J., *J. Am. Cer. Soc.*, **77** (1994) 431.
21. Mayer, J., Flynn, C. P. & Rühle, M., *Ultramicroscopy*, **33** (1989) 51.
22. Mayer, J., Gutekunst, G., Möbus, G., Dura, J., Flynn, C. P. & Rühle, M., *Acta Metall. Mater.*, **40** (1992) S227.
23. Gutekunst, G., Mayer, J. & Rühle, M., *Scripta Metall. Mater.*, **31** (1994) 1097.
24. Gutekunst, G., Mayer, J. & Rühle, M., *Atomic Structures of Expitaxial Nb/Al_2O_3 Interfaces: I. Coherent Regime*, to be published.
25. Vitek, V., Gutekunst, G., Mayer, J. & Rühle, M., *Phil. Mag.*, **A71** (1995) 1219.
26. Tricker, D. M. & Stobbs, W. M., *Phil. Mag.*, **A71** (1995) 1037 & 1051.
27. Gutekunst, G., Mayer, J. & Rühle, M., *Atomic Structure of Epitaxial Nb/Al_2O_3 Interfaces: II. Misfit Dislocations*, to be published.
28. Elßner, G., Korn, D. & Rühle, M., *Scripta Metall. Mater.*, **31** (1994) 1037.
29. Korn, D., Elßner, G. & Rühle, M., to be published.
30. Rühle, M., *Fundamentals of Metal-Matrix Composites*, eds S. Suresh, A. Mortensen & A. Needleman, Butterworth-Heinemann, Boston, 1993, p. 81.
31. Hirsch, P. B., Howie, A., Nicholson, R., Pahsley, D. W. & Whelan, M. J., *Electron Microscopy of Thin Crystals*, Krieger Publishers Company, Malobar/FL, USA
32. Joy, D. C., Ronnig, Jr., A. D. & Goldstein, J. I. (eds), *Principles of Analytical Electron Microscopy*, Plenum Press, New York, 1979.
33. Egerton, R. F., *Electron Energy-Loss Spectroscopy*, Plenum Press, New York, 1986.
34. Disko, M. M., Ahn, C. C. & Fultz, B., (eds.), *Transmission Electron Energy Loss Spectroscopy in Materials Science*, The Minerals, Metals and Materials Society, Warrendale, 1992.
35. Bruley, J., *Microsc. Microanal. Microstruc.*, **4** (1993) 23.
36. Spence, J. C. H., *Experimental High-Resolution Electron Microscopy*, 2nd ed., Oxford University Press, New York and Oxford, 1988.
37. Busek, P., Cowley, J. & Eyring, L. (eds), *High-Resolution Transmission Electron Microscopy*, Oxford University Press, New York and Oxford, 1988.
38. Horiuchi, S., *Fundamentals of High-Resolution Electron Microscopy*, North Holland Publishing Company, Amsterdam, (1993).
39. Phillipp, F., Höschen, R., Möbus, G., Osaki, M. & Rühle, M., *Ultramicroscopy*, **56** (1994) 1.
40. Frank, J. (ed.), *Electron Tomography*, Plenum Press, New York and London, 1992.
41. Möbus, G. & Rühle, M., *Optik*, **93** (1993) 108.
42. Möbus, G, Necker, G. & Rühle, M., *Ultramicroscopy*, **49** (1993) 46.
43. Hofmann, D. & Ernst, F., *Ultramicroscopy*, **56** (1994) 54.
44. Möbus, G. & Rühle, M., *Ultramicroscopy*, **56** (1994) 54.
45. Frank, J., *Computer Processing of Electron Microscopy Images*, ed. P. W. Hawkes, Springer-Verlag Berlin, 1980, p. 235.
46. Durbin, S. M., Cunningham, J. E., Mochel, M. E. & Flynn, C. P., *J. Phys.*, **F11** (1981) L223.
47. Lee, W. E. & Lagerlöf, K. P. D., *J. Electron. Microsc. Tech.*, **2** (1985) 247.
48. Bruley, J., Brydson, R., Müllejans, H., Mayer, J., Gutekunst, G., Mader, W., Knauss, D., & Rühle, M., *J. Mater. Res.*, **9** (1994) 2574.
49. Thölen, A. R., *Phys. Stat. Sol. (a)*, **2** (1970) 537.
50. Ernst, F., Pirouz, P. & Heuer, A. H., *Phil. Mag.*, **A63** (1990) 259.
51. Dehm, G., Rühle, M., Ding, G. & Raj, R., *Phil. Mag.*, **A71** (1995) 1111.